

# Genetic-algorithm-aided ultra-broadband perfect absorbers using plasmonic metamaterials

Alexandre Mayer,<sup>†,#</sup> Hai Bi,<sup>‡,¶</sup> Sarah Griesse-Nascimento,<sup>‡</sup> Benoit Hackens,<sup>§</sup>  
 Jérôme Loicq,<sup>||,⊥</sup> Eric Mazur,<sup>‡</sup> Olivier Deparis,<sup>†</sup> and Michaël Lobet<sup>\*,†,||,‡,#</sup>

<sup>†</sup>*Laboratoire de Physique du Solide, University of Namur, Rue de Bruxelles 61, 5000  
 Namur, Belgium*

<sup>‡</sup>*John A. Paulson School of Engineering and Applied Sciences, Harvard University, 9  
 Oxford Street, Cambridge, MA 02138, United States of America*

<sup>¶</sup>*Ji Hua Laboratory, Island Ring South Street, Foshan, Guangdong 528000, P. R. China*

<sup>§</sup>*IMCN/NAPS, Université catholique de Louvain (UCLouvain), 1348 Louvain-la-Neuve,  
 Belgium*

<sup>||</sup>*Centre Spatial de Liège, Avenue du Pré-Aily, 4031 Angleur, Belgium*

<sup>⊥</sup>*Faculty of Aerospace Engineering, Delft University of Technology, Delft, 2629 HS,  
 Netherlands*

*#These authors contributed equally to this work.*

E-mail: michael.lobet@unamur.be

## Abstract

Complete absorption of electromagnetic waves is paramount in today's applications, ranging from photovoltaics to cross-talk prevention into sensitive devices. In this context, we use a genetic algorithm (GA) strategy to optimize absorption properties of periodic arrays of truncated square-based pyramids made of alternating stacks

of metal/dielectric layers. We target ultra-broadband quasi-perfect absorption of normally incident electromagnetic radiations in the visible and near-infrared ranges (wavelength comprised between 420 and 1600 nm). We compare the results one can obtain by considering one, two or three stacks of either Ni, Ti, Al, Cr, Ag, Cu, Au or W for the metal, and poly(methyl methacrylate) (PMMA) for the dielectric. More than  $10^{17}$  configurations of geometrical parameters are explored and reduced to a few optimal ones. This extensive study shows that Ni/PMMA, Ti/PMMA, Cr/PMMA and W/PMMA provide high-quality solutions with an integrated absorptance higher than 99% over the considered wavelength range, when considering realistic implementation of these ultra-broadband perfect electromagnetic absorbers. Robustness of optimal solutions with respect to geometrical parameters is investigated and local absorption maps are provided. Moreover, we confirm that these optimal solutions maintain quasi-perfect broadband absorption properties over a broad angular range when changing the inclination of the incident radiation. The study also reveals that noble metals (Au, Ag, Cu) do not provide the highest performance for the present application.

## Keywords

Ultra-broadband absorption, plasmonic metamaterials, genetic algorithm

## Introduction

Since its theoretical introduction in 1860 by G. Kirchhoff, the black body concept played a seminal role in the history of quantum mechanics and modern physics.<sup>1</sup> It originally referred to an *idealized physical body of infinitely small thickness, that completely absorbs all incident rays, and neither reflects nor transmits any.*<sup>2</sup> The modern acceptance of the term does not include the infinitely small thickness anymore but still preserves the requirement to absorb all incident electromagnetic radiation regardless of the wavelength, the polarization or the angle of incidence of the incoming radiation. First experimental realizations of black bodies

at the end of the 19th century/ dawn of the 20th century consisted of metallic boxes with its interior walls blackened by mixed chromium, nickel and cobalt oxides.<sup>3-5</sup> The quest for a Perfect Electromagnetic Absorber (PEA), i.e. the materialization of the idealized black body, continued over the years for example due to the recent need of efficient solar energy harnessing or camouflage solutions, the development of photothermal detectors or in order to prevent crosstalk in nanoscale opto-electronics and quantum technologies.<sup>6,7</sup> Among efficient solutions, carbon black and carbon nanotubes materials provide ultra-broadband PEA with 98-99 % absorption from UV to far infrared<sup>8</sup> while nickel-phosphorus alloy reach 96 % on the  $5 - 9\mu m$  range.<sup>9</sup>

At the dawn of the present century, metamaterials and plasmonic materials provided new opportunities in order to mold the flow of light at the nanoscale and drastically enhance light-matter interactions.<sup>10-13</sup> Negative refraction, cloaking, superlensing, near-zero refractive index, surface enhanced Raman scattering, high energy concentrations at metal-dielectric interfaces are some examples of current interest among those hot topics in photonics.<sup>14-16</sup> Nevertheless, losses due to metallic components are an important drawback limiting current applications.<sup>17</sup> This drawback was turned into an advantage by Landy *et al.* who designed the first metamaterial PEA by using metallic resonators operating at a single wavelength.<sup>18</sup> The metamaterial approach was successfully applied during the last decade in order to tame the black body radiation and provide efficient PEA over a broad range of frequencies.<sup>19-34</sup> Some proposed theoretical structures are nevertheless facing some technological difficulties due to the current limitations in resolution and complexity of the structures, especially in the visible range. The field of plasmonic metamaterials PEA is now mature enough to enter a novel phase of *in silico* modeling in order to develop more realistic PEA,<sup>35-37</sup> while preserving the ultra-broadband character of the PEA as well as its low angular dependency.

Here, we report on ultra-broadband metamaterial PEA using periodic stacks of square metal/dielectric layers arranged in a pyramidal way (see Fig. 1). We investigate among twenty-four possible PEA which are realistic from an experimental point of view and based

on eight common metals arranged either in one, two or three stacks of metal/dielectric layers. The fact that the number of layers is limited to a few ones, while preserving the performances, is attractive in view of the tradeoff between fabrication complexity and broad absorption properties. It provides realistic perspectives for device fabrication with current technology. No less than  $10^{17}$  configurations are explored by varying different experimental parameters such as the lateral size of the metal/dielectric layers, the thickness of the dielectric layer or the lateral periodicity between different individual structures. The search for the optimal configuration, i.e. the PEA with the largest absorptance of electromagnetic (EM) radiations over the visible to mid-infrared (MIR) range, is realized using a Genetic Algorithm (GA) strategy. Optimal configurations are reported as well as their absorptance spectra. Moreover, fields maps and angular dependency of the optimal PEA are discussed. The latter is primordial for several applications of black coatings such as cross-talk prevention in qubits.<sup>6,7</sup> or stray light reduction.<sup>38,39</sup>

## Design

Energy conservation imposes that reflectance  $R$ , transmittance  $T$  and absorptance  $A$  are related through

$$R(\lambda, \theta) + T(\lambda, \theta) + A(\lambda, \theta) = 1 \quad (1)$$

with  $\lambda$  being the wavelength of the incident EM radiation and  $\theta$  the angle of incidence. Maximizing absorption requires suppressing both transmission and reflection at the same time. The PEA can be made opaque, i.e. no transmission, by adding a metallic layer over the substrate. In order to lower the reflection, the PEA needs to be impedance matched. Surface corrugations in a tapered way provide this gradual transition between the refractive indices of both incidence and substrate media. This anti-reflection strategy is well-known both in Nature or in transparent coatings.<sup>40,41</sup> The previous approach leads to suppressed transmission ( $T = 0$ ) and drastically reduced reflection ( $R \rightarrow 0$ ). To minimize reflection and

fully absorb the incident radiation in order to obtain a PEA, the energy transported by the radiation has to be dissipated through the excitation of eigenmodes of the structure. This can be done for example by exciting localized surface plasmons (LSP) at the interfaces of metal/dielectric square resonators.<sup>42-45</sup> The wavelength associated with these plasmonic resonances is proportional to the lateral dimensions of the metallic layers, conferring the desired broadband character once metallic resonators of varied sizes are stacked. Following this approach, truncated square-based pyramids made of twenty stacks of Au/Ge layers lead to an integrated absorptance of 98% of normally incident radiations over a 0.2-5.8  $\mu\text{m}$  wavelength range.<sup>46,47</sup> However, fabrication of such elaborated structures, with nanometer resolution and high number of layers is currently too demanding in terms of time and resources.

There is thus a need for simplified structures to reach ultra-broadband PEA that are tractable experimentally. Therefore, we consider here a simpler PEA consisting of one, two or three stacks of metal/dielectric layers (see Fig. 1).<sup>35,36</sup> We set the thickness of all metal layers within the pyramid stack to 15 nm,<sup>46</sup> which is smaller than the skin depth of the metals considered over the targetted radiation wavelength range, i.e. from 420 to 1600 nm here. It allows therefore a coupling between the surface plasmons at the two sides of each metallic layer. Moreover, we consider poly(methyl methacrylate) (PMMA) as dielectric.<sup>35,36,48</sup> PMMA can be easily deposited using spin-coating techniques and its thickness can be simply varied by changing PMMA/solvent relative concentration in solution, or spinning speed for example.

A vast range of metals are considered in the present study, namely Ni, Ti, Al, Cr, Ag, Cu, Au or W.<sup>49-52</sup> Those metals correspond to widely used materials in current nanophotonics applications, and are readily deposited to form few nm-thick films through physical deposition techniques. The thickness  $t_i$  of each dielectric layer and the lateral dimension  $L_i$  of each metal/dielectric stack are adjustable parameters in the present GA-aided approach. The lateral periodicity  $P$  of the system also remains an adjustable parameter. This relaxation of the PEA dimensions, as compared with previous studies<sup>46</sup> where thickness was the same for

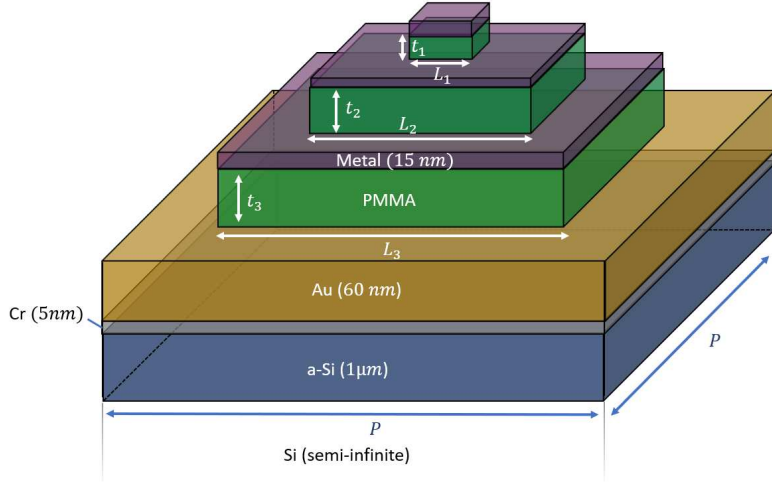


Figure 1: Perfect Electromagnetic Absorber using square-based truncated pyramid made of  $N = 1, 2$  or  $3$  stacks of metal/PMMA layers. PMMA thickness  $t_i$  and size  $L_i$  of each layer is optimized using a Genetic Algorithm strategy, as well as the period  $P$  of the PEA. The support of the pyramid consists of uniform layers of Au (60 nm), Cr (5 nm) and a-Si (1 micron); they rely on an infinite substrate of Si ( $\varepsilon = 16$ ).

all metallic layers and for all dielectric layers, provides the extra degrees of freedom that are necessary to maintain high performances while reducing the number of metallic layers.

The role of these different parameters can be understood as follows. The lateral dimensions  $L_i$  of the metallic resonators essentially control the plasmonic resonances of the system. The thicknesses  $t_i$  of the dielectric layers control the vertical coupling between these resonators while the periodicity  $P$  finally controls the lateral coupling between the pyramids.<sup>46</sup> The detailed variation range of these parameters are provided in SI. Furthermore, the PEA stands on a flat 60 nm-thick gold layer that blocks the transmission of the considered incident radiations and reflects any EM radiation not absorbed in the pyramids. This gold layer stands on a 5-nm thick chromium (Cr) adhesion layer followed by a 1  $\mu\text{m}$ -thick amorphous silicon (a-Si) layer. We consider finally a semi-infinite Si substrate ( $\varepsilon = 16$ ). This choice of a silicon substrate has no impact on our results since no radiation will actually reach this region.

## Optimization schemes

For a system made of  $N$  stacks of metal/dielectric layers, we consequently have a total of  $2N+1$  parameters to consider (i.e.,  $L_i$ ,  $t_i$  and  $P$  for  $i \in [1, N]$ ). Different methods are used in optics to determine optimal parameter combinations. The systematic evaluation of a whole grid of possible parameter combinations is generally limited to two or three parameters. Local optimization methods such as the (quasi-)Newton method or gradient descent are more efficient in terms of the required number of function evaluations.<sup>53</sup> They converge however generally to the first local optimum encountered. Global optimization methods are preferable in this respect since they provide a wider exploration of the parameter space, which can eventually lead to higher-quality solutions (ideally the best-possible solution). Genetic Algorithms (GA),<sup>54-56</sup> Particle Swarm Optimization (PSO)<sup>57-59</sup> and Ant Colony Optimization (ACO)<sup>60</sup> are popular global optimization methods that rely on a collective exploration of the parameter space. The population dynamics of these algorithms is inspired by the principles of natural selection for GA, birds flocks dynamics for PSO or pheromone-guided exploration for ACO. These methods can easily escape local optima and find higher-quality solutions. They do not require the calculation of gradients. They are intrinsically suited to a parallel computing, since the fitness of each individual in the population can be evaluated independently. Machine Learning (ML) techniques such as deep neural networks or autoencoders can help the search by learning representations of the function to optimize.<sup>61</sup>

We use in this work a home-made genetic algorithm (see workflow in Fig. 2 and the Supplementary Material for a detailed description) to address this optimization problem and establish realistic structures that consist of only one, two or three stacks of metal/dielectric layers. We consider in particular poly(methyl methacrylate) (PMMA) for the dielectric and either Ni, Ti, Cr, Al, Ag, Cu, Au or W for the metal (eight possible materials). This makes a total of  $24=3 \times 8$  structures (1 to 3 layers, 8 metals) that are optimized with the objective to maximize the absorption of normally incident radiations with wavelengths comprised between 420 and 1600 nm.

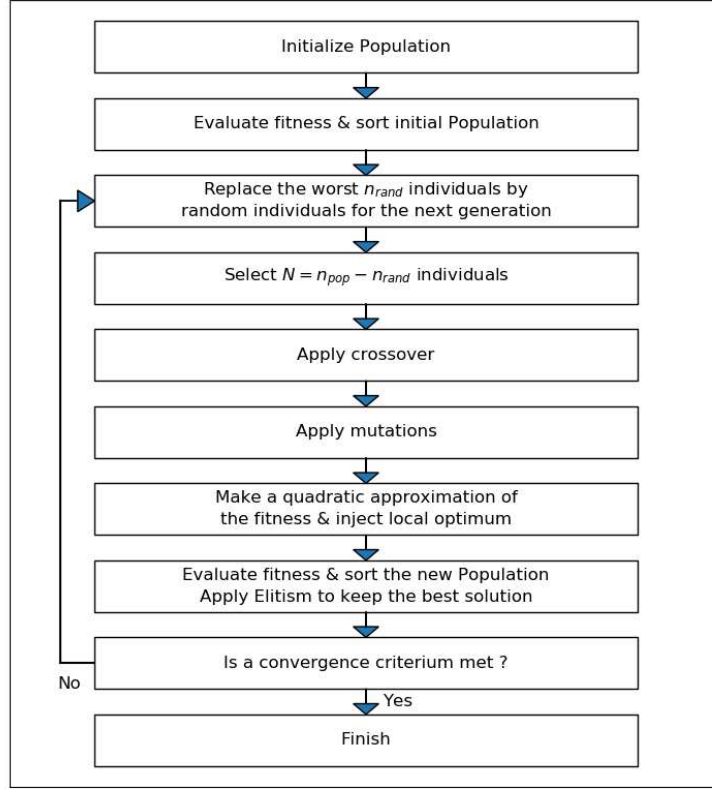


Figure 2: Workflow of the Genetic Algorithm.

The objective function to be maximized (also called fitness or figure of merit) will be the integrated absorptance for normally incident radiations with wavelengths comprised between 420 and 1600 nm. It is formally defined by  $\eta(\%) = 100 \times \frac{\int_{\lambda_{\min}}^{\lambda_{\max}} A(\lambda) d\lambda}{\lambda_{\max} - \lambda_{\min}}$ , where  $A(\lambda)$  refers to the absorptance of normally incident radiations at the wavelength  $\lambda$ ,  $\lambda_{\min}=420$  nm and  $\lambda_{\max}=1600$  nm. This is the quantity that the Genetic Algorithm seeks at maximizing by exploring the geometrical parameters of the structure considered. It relies on an homemade Rigorous Coupled Waves Analysis (RCWA) code that solves Maxwell's equations exactly for stratified periodic systems.<sup>41,62</sup> A plane wave (PW) expansion of the electric permittivity of the PEA is made, in which the number of Fourier components is the key parameter to insure numerical convergence.



## Results and discussion

Once the GA started, one can follow generation after generation the fitness of the best individual in the population as well as the mean fitness in the population. The best fitness usually increases rapidly in the first generations as better solutions are rapidly detected. Progress becomes typically slower after these first generations as the algorithm must either escape a local optimum to detect a radically different solution (exploration) or refine the best solution found so far to finalize the optimization (exploitation). A good optimization algorithm must actually find a sound balance between these two aspects. The mean fitness of the population follows the best fitness, to a degree that depends on the convergence of the population to the best individual, convergence measured by the genetic similarity  $s$  defined in SM. Fig. 3 shows the best fitness and the mean fitness achieved in the first 80 generations, when optimizing  $N = 3$  stacks of W/PMMA. All optimizations are actually carried out by using  $11 \times 11$  plane waves in the RCWA simulations. The figure also shows the absorptance spectrum for the best solutions found by the genetic algorithm after 0, 5, 10, 18, 233 and 339 generations. High-quality solutions are established rapidly by the GA in the first generations ( $\eta = 97.7\%$  at generation 0,  $98.8\%$  at generation 5,  $99.0\%$  at generation 10 and  $99.3\%$  at generation 18). Qualitative improvements become then slower. The final solution ( $\eta=99.4\%$ ) is found after 339 generations in this case.

Fig. 4 shows the best fitness (integrated absorptance  $\eta$ ) achieved for the different structures considered. These results correspond to  $N = 1, 2$  and 3 stacks of metal/dielectric layers and the eight different metals considered in this study. They correspond to the  $3 \times 8 = 24$  systems actually optimized by the Genetic Algorithm (the optimization relies on RCWA calculations with  $11 \times 11$  plane waves; the final solutions are confirmed by considering  $21 \times 21$  plane waves). This extensive study reveals that Ni, W, Cr or Ti represent the best materials for this application. It is noticeable that integrated absorptance values above  $86.1\%$  are achieved for the  $3 \times 4 = 12$  optimized structures that correspond to these four metals. The best structures, which consist of  $N = 3$  stacks of Ni, W, Cr or Ti/PMMA layers, have

all an integrated absorptance above 99%. Those results are, to the best of our knowledge, the best PEA proposed in recent literature over such an extended wavelength range in the visible and NIR. The geometrical parameters and the figure of merit obtained for the four best metals selected (Ni, W, Cr and Ti) are given in Table 1. The results that correspond to the other four metals (Al, Cu, Au and Ag) are given in Table 2. They will be discarded for this PEA application, essentially because of a lack of robustness of these solutions within the parameter space, i.e. sensitivity to experimental deviations, in addition to lower integrated absorptance values. It should be noted that three out of those four less convincing are noble metals (Cu, Au, Ag) and are usually considered as low-loss metals for plasmonic applications.<sup>17,63</sup> Considering that the choice of noble metals (Au, Ag, Cu) impacts on fabrication costs, it is interesting to note that they do not provide the highest performance for the present application.

High-quality solutions must actually meet two requirements in order to be easily implemented in real devices: (i) to provide the highest possible integrated absorptance  $\eta$ , but also (ii) to be robust with respect to slight variations of the geometrical parameters (compatibility with fabrication tolerances). We ideally want to find a broad optimum rather than a sharp one. When running the GA to find optimal geometrical parameters, it is possible to interpolate the data collected by the algorithm and establish maps of the fitness in 2-D planes that cross the  $n$ -dimension point finally established by the GA. These maps reveal the robustness of the final solution (i.e., its stability with respect to slight variations of the geometrical parameters). An example is given in Fig. 5, where we compare the maps obtained when optimizing  $N = 1$  stack of Ni/PMMA (broad optimum - Fig. 5(a)-(b-)) and  $N = 1$  stack of Au/PMMA (sharp optimum - Fig. 5(c)-(d)). These maps reveal that the solution found for Ni/PMMA is actually robust for practical applications, while the solution found for Au/PMMA is too sensitive. For  $N=1$  stack of Ni/PMMA,  $P$ ,  $L_1$  and  $t_1$  have indeed a domain of variation of 82 nm, 51 nm and 71 nm respectively around the optimum (domain associated with  $\eta \geq \eta_{\text{opt}} - 5\%$ ). For  $N=1$  stack of Au/PMMA, this domain is reduced to 21

Table 1: Geometrical parameters and figure of merit  $\eta$  for optimal structures made of  $N = 1, 2$  or  $3$  stacks of Ni/PMMA, W/PMMA, Cr/PMMA or Ti/PMMA (from top to bottom). PW: number of plane waves used in the calculations of  $\eta$ .

Ni / PMMA

	$L_1$ (nm)	$t_1$ (nm)	$L_2$ (nm)	$t_2$ (nm)	$L_3$ (nm)	$t_3$ (nm)	$P$ (nm)	$\eta_{11 \times 11 \text{PW}}$	$\eta_{21 \times 21 \text{PW}}$
$N = 1$ stack	201	117	-	-	-	-	286	95.0%	93.8%
$N = 2$ stacks	132	123	227	107	-	-	287	99.4%	99.0%
$N = 3$ stacks	149	131	268	124	369	101	412	99.8%	<b>99.3%</b>

W / PMMA

	$L_1$ (nm)	$t_1$ (nm)	$L_2$ (nm)	$t_2$ (nm)	$L_3$ (nm)	$t_3$ (nm)	$P$ (nm)	$\eta_{11 \times 11 \text{PW}}$	$\eta_{21 \times 21 \text{PW}}$
$N = 1$ stack	250	115	-	-	-	-	333	85.8%	86.1%
$N = 2$ stacks	222	127	368	119	-	-	419	98.0%	98.0%
$N = 3$ stacks	152	117	266	122	379	125	419	99.4%	<b>99.2%</b>

Cr / PMMA

	$L_1$ (nm)	$t_1$ (nm)	$L_2$ (nm)	$t_2$ (nm)	$L_3$ (nm)	$t_3$ (nm)	$P$ (nm)	$\eta_{11 \times 11 \text{PW}}$	$\eta_{21 \times 21 \text{PW}}$
$N = 1$ stack	314	124	-	-	-	-	419	88.8%	88.7%
$N = 2$ stacks	192	121	332	127	-	-	369	98.5%	98.5%
$N = 3$ stacks	151	120	277	127	427	123	467	99.4%	<b>99.1%</b>

Ti / PMMA

	$L_1$ (nm)	$t_1$ (nm)	$L_2$ (nm)	$t_2$ (nm)	$L_3$ (nm)	$t_3$ (nm)	$P$ (nm)	$\eta_{11 \times 11 \text{PW}}$	$\eta_{21 \times 21 \text{PW}}$
$N = 1$ stack	368	134	-	-	-	-	491	89.3%	88.9%
$N = 2$ stacks	175	117	306	127	-	-	336	98.6%	98.5%
$N = 3$ stacks	161	125	302	126	451	113	491	99.4%	<b>99.0%</b>

nm, 10 nm and 91 nm respectively. The lateral dimension  $L_1$  is the most sensitive parameter in this case. All solutions presented in Table 1 were checked for their robustness, based on the inspection of the fitness maps established by the GA. They appeared to correspond to broad optima suitable for practical applications. On the contrary, the solutions presented in Table 2 were discarded because they actually correspond to sharp optima.

A quality check of the reliability of the presented solutions is performed by increasing the plane wave number to  $21 \times 21$  (see Table 1 and 2 and extended discussion in SM). This quality check allows us to further confirm the stability of our results: while increasing the plane wave number, good solutions (Table 1 - Ni;W;Cr;Ti) are stable regarding the  $\eta$  parameter (deviation of  $\eta$  limited to 1.2%, when comparing  $11 \times 11$  and  $21 \times 21$  PW), while less optimal ones (Table 2 - Al;Cu;Au;Ag) are much less stable (deviation of  $\eta$  between 8.1%

Table 2: Geometrical parameters and figure of merit  $\eta$  for optimal structures made of  $N = 1, 2$  or  $3$  stacks of Al/PMMA, Cu/PMMA, Au/PMMA or Ag/PMMA (from top to bottom). PW: number of plane waves used in the calculations of  $\eta$ .

Al / PMMA

	$L_1$ (nm)	$t_1$ (nm)	$L_2$ (nm)	$t_2$ (nm)	$L_3$ (nm)	$t_3$ (nm)	$P$ (nm)	$\eta_{11 \times 11 \text{PW}}$	$\eta_{21 \times 21 \text{PW}}$
$N = 1$ stack	221	151	-	-	-	-	491	89.2%	<b>63.8%</b>
$N = 2$ stacks	187	108	263	58	-	-	415	97.9%	<b>81.0%</b>
$N = 3$ stacks	129	112	208	110	294	97	465	98.7%	<b>83.6%</b>

Cu / PMMA

	$L_1$ (nm)	$t_1$ (nm)	$L_2$ (nm)	$t_2$ (nm)	$L_3$ (nm)	$t_3$ (nm)	$P$ (nm)	$\eta_{11 \times 11 \text{PW}}$	$\eta_{21 \times 21 \text{PW}}$
$N = 1$ stack	149	112	-	-	-	-	230	80.9%	<b>55.2%</b>
$N = 2$ stacks	188	127	283	120	-	-	447	89.1%	<b>75.8%</b>
$N = 3$ stacks	119	145	211	132	299	111	365	95.5%	<b>77.5%</b>

Au / PMMA

	$L_1$ (nm)	$t_1$ (nm)	$L_2$ (nm)	$t_2$ (nm)	$L_3$ (nm)	$t_3$ (nm)	$P$ (nm)	$\eta_{11 \times 11 \text{PW}}$	$\eta_{21 \times 21 \text{PW}}$
$N = 1$ stack	196	160	-	-	-	-	416	68.5%	<b>52.5%</b>
$N = 2$ stacks	158	152	267	89	-	-	326	85.5%	<b>65.1%</b>
$N = 3$ stacks	172	79	202	110	335	100	409	91.2%	<b>70.4%</b>

Ag / PMMA

	$L_1$ (nm)	$t_1$ (nm)	$L_2$ (nm)	$t_2$ (nm)	$L_3$ (nm)	$t_3$ (nm)	$P$ (nm)	$\eta_{11 \times 11 \text{PW}}$	$\eta_{21 \times 21 \text{PW}}$
$N = 1$ stack	152	112	-	-	-	-	235	43.9%	<b>35.8%</b>
$N = 2$ stacks	179	144	303	108	-	-	369	57.1%	<b>42.9%</b>
$N = 3$ stacks	101	151	193	155	268	110	330	66.1%	<b>46.4%</b>

and 25.7%, when comparing  $11 \times 11$  and  $21 \times 21$  PW).

Fig. 6 represents the absorptance spectrum obtained for normally incident radiations with the four best structures identified in this work ( $N = 3$  stacks of Ni/PMMA, W/PMMA, Cr/PMMA or Ti/PMMA). These structures provide respectively an integrated absorptance  $\eta$  of 99.3%, 99.2%, 99.1% and 99.0% (results for RCWA calculations using  $21 \times 21$  plane waves). These results are amongst the best reported so far in the literature and confirm that the initial goal of designing an ultra-broadband PEA in the visible-NIR range is met. The challenge of fabricating such PEA is mitigated by the small number of layers and the selection of metals that are better alternatives to noble metals. Moreover, the proposed PEA are robust with respect to fabrication tolerances.

## Plasmonic absorber characteristics

In order to better describe the physics of those PEA, we will focus from now on only on the best structure identified in this work, i.e. the one made of  $N = 3$  stacks of Ni/PMMA. It provides an integrated absorptance of 99.3%. As shown above, the solution is robust with respect to deviations of the geometrical parameters (broad optimum), as confirmed by 2-D maps of the fitness around the optimum and the comparison between the results obtained with  $11 \times 11$  and  $21 \times 21$  plane waves.

We can calculate the Poynting vector  $\vec{S} = \frac{1}{2} \vec{E} \times \vec{H}^*$ , where  $\vec{E}$  and  $\vec{H}$  refer here to the complex-number representation of the electric and magnetic fields, in order to show the energy flow through the structure. Moreover, we can determine the local absorption inside the PEA. Based on the method developed by Brenner,<sup>64</sup> the absorbed power  $P_a$  in a volume  $V$  can be estimated by

$$P_a = \frac{\varepsilon_0 \omega}{2} \int_V \text{Im}(\varepsilon(\mathbf{r}, \omega)) |\mathbf{E}(\mathbf{r}, \omega)|^2 dV \quad (2)$$

with  $\varepsilon(\mathbf{r}, \omega)$  the local complex electric permittivity. By normalizing the absorbed power  $P_a$  to the incident power  $P_i$ , one obtains the local absorptance  $A_{loc}(\mathbf{r}, \omega) = P_a/P_i$ .

These calculations provide additional physical insight by showing in which parts of the structure the incident radiations are absorbed. An example is provided in Fig.7 for a normally incident radiation at a wavelength of 1000 nm. These results show that this radiation is essentially absorbed in the second metallic layer (25.9% of the incident radiation is absorbed in the top metallic layer, 50.3% in the central metallic layer and 23.3% in the bottom metallic layer). This is totally consistent with our previous work showing that the lower (upper) part of the pyramid absorbs higher (lower) wavelength,<sup>46</sup> as predicted by the variation of LSP with the size of the resonators.

The results presented so far concerned the absorption of normally incident radiations. However, in many applications such as stray light mitigation, the PEA should be stable from

an angular point of view. Therefore, we check how the integrated absorptance  $\eta$  for  $N = 3$  stacks of Ni/PMMA depends on the polar and azimuthal angles ( $\theta$  and  $\phi$ ) of the incident radiation. These results are presented in Fig. 8. The left part of this figure provides a complete 2-D map of the integrated absorptance with respect to the polar and azimuthal angles of the incident radiation. This map is actually generated by a cubic interpolation of data computed for only 73 points (blue points in the representation). The right part of this figure shows an horizontal section ( $\theta \in [-90^\circ, 90^\circ]$  and  $\phi = 0^\circ$ ) for incident radiations that are either  $s$ -polarized (TE),  $p$ -polarized (TM) or unpolarized ( $\frac{1}{2}(\text{TE}+\text{TM})$ ). These results show that the integrated absorptance  $\eta(\theta, \phi)$  remains quasi-perfect over a broad angular domain ( $\eta(\theta, \phi) \geq 98.5\%$  for  $\theta \leq 40^\circ$ ). This makes the proposed solution for a broadband quasi-perfect absorber made of three stacks of Ni/PMMA extremely robust for practical applications also from an angular point of view. Fig. 9 finally shows the horizontal profiles achieved when considering  $N = 3$  stacks of Ni/PMMA, W/PMMA, Cr/PMMA or Ti/PMMA, i.e. for the four best solutions identified in this work, in the case of an unpolarized incident radiation. This figure confirms the exceptional robustness of these best four solutions with respect to the inclination of the incident radiation.

## Conclusion

Numerical investigations of truncated square-based pyramids made of a few number (one to three) of alternating stacks of metal/dielectric layers are carried out. We focused on realistic configurations consisting of maximum three metallic layers stacked above each other. The GA strategy allowed to explore  $10^{17}$  geometrical configurations and selected the optimal ones. Ni/PMMA, W/PMMA, Cr/PMMA and Ti/PMMA are determined as the best configurations for realizing PEA over the visible and NIR range, with integrated absorption higher than 99 % once three layers are considered. Those PEA are robust against geometrical parameter deviations that might occur during experimental realization. Moreover,

these optimal solutions maintain quasi-perfect broadband absorption properties over a broad angular range when changing the incidence angle of EM radiation. This study offers guidelines for a realistic design of PEA, that can readily be fabricated using currently available micro/nanofabrication techniques, using modest resources.

## Acknowledgement

The authors would like to thank N. Reckinger and L. Henrard for stimulating discussions. A.M. and B.H. are funded by the Fund for Scientific Research (F.R.S.-FNRS) of Belgium. A.M. is member of NaXys, Namur Institute for Complex Systems, University of Namur, Belgium. This research used resources of the “Plateforme Technologique de Calcul Intensif (PTCI)” (<http://www.ptci.unamur.be>) located at the University of Namur, Belgium, which is supported by the F.R.S.-FNRS under the convention No. 2.5020.11. The PTCI is member of the “Consortium des Equipements de Calcul Intensif (CECI)” (<http://www.ceci-hpc.be>). The present research also benefited from computational resources made available on the Tier-1 supercomputer of the Fédération Wallonie-Bruxelles, infrastructure funded by the Walloon Region under the grant agreement No. 1117545. Part of this work was performed while M.L. was a recipient of a Fellowship of the Belgian American Educational Foundation.

## Supporting Information Available

### Range of variation of the parameters for the Genetic Algorithm

We consider that the lateral periodicity  $P$  of the system can take values between 50 and 500 nm (by steps of 1 nm). The lateral dimension  $L_i$  of each stack of metal/dielectric layers can take values between 50 and 500 nm (by steps of 1 nm). The thickness  $t_i$  of each dielectric can take values between 50 and 250 nm (by steps of 1 nm). The subscripts  $i=1, 2$  and  $3$  refer respectively to the stack at the apex, in the middle or at the bottom of each nanopillar (Fig. 1). In order to obtain pyramidal structures, we require that the final

solution satisfies  $L_1 < L_2 < L_3 \leq P - 40$  nm, where 40 nm represents the minimal imposed safe distance between adjacent pyramids for insuring realistic fabrication. When optimizing structures made of three stacks of metal/dielectric layers, there are actually seven parameters to determine ( $P, L_1, t_1, L_2, t_2, L_3$  and  $t_3$ ), with a total of 13,936,405,106,594,025 possible parameter combinations to consider if the relaxed constraint  $L_1 < L_2 < L_3 \leq P$  is actually enforced during the optimization.

### Description of the Genetic Algorithm

Given  $n$  decision variables  $x_i \in [x_i^{\min}, x_i^{\max}]$  to determine (within a precision  $\Delta x_i$  representative of experimental constrains on the fabrication of a device), the objective is to find the global maximum of an objective function  $f = f(x_1, \dots, x_n)$ . The variables  $x_i$  are encoded by sequences of binary digits (genes), which actually represent in the original Gray code the number of steps  $(x_i - x_i^{\min})/\Delta x_i$  between  $x_i^{\min}$  and  $x_i$ .<sup>56</sup> We refer by DNA to a complete set of  $n$  genes. We work with a population of  $n_{\text{pop}}=50$  individuals. The initial population consists of random individuals. At each generation, we evaluate in parallel the fitness  $f(x_1, \dots, x_n)$  of new individuals. We keep a record with all fitness evaluations in order to avoid any duplication of these evaluations. The population is sorted from the best individual to the worst. The worst  $n_{\text{rand}}$  individuals are replaced by random individuals in the next generation. We use  $n_{\text{rand}} = 0.1 \times n_{\text{pop}} \times (1 - p)$ , where  $p = |s - 0.5|/0.5$  is a progress indicator and  $s$  is the genetic similarity (fraction of bits in the population whose value is identical to the best individual). The remaining part of the population ( $N = n_{\text{pop}} - n_{\text{rand}}$  individuals) participate to the steps of selection, crossover and mutation.

The core operations of the Genetic Algorithm are the following. *Selection*:  $N$  parents are selected from a population of  $N$  individuals by a rank-based roulette wheel selection, noting that a given individual can be selected several times.<sup>56</sup> *Crossover*: For any pair of parents, we define two children for the next generation either (i) by a crossover operation (probability of 70%), or (ii) by a simple replication of the parents (probability of 30%). In the current version



of our GA, the crossover operation can be a binary one-point crossover<sup>1</sup> between the DNA of the two parents<sup>36</sup> (probability  $p_{\text{bin}}$  of 0.8 initially) or a real-valued crossover<sup>2</sup> between the variables  $\vec{x}$  represented by the two parents (probability of  $1 - p_{\text{bin}}$ ).  $p_{\text{bin}}$  is adapted according to the success of these operators. *Mutation*: The children obtained by crossover are subjected to mutations. This operation consists of a random flipping of the binary digits of a DNA. The probability of individual bit flips is set to  $m = 0.95/n_{\text{bits}}$ , where  $n_{\text{bits}}$  is the number of bits in a DNA. In order to increase the diversity of the displacements generated by these mutations, we actually express the gene values in randomly-shifted versions of the original Gray code and apply the mutations to these encodings (see Appendix A of Ref. 35 for details). In the current version of our GA, mutations can be "isotropic" (in this case, the mutation operator is applied  $n$  times on a given DNA). The probability  $p_{\text{iso}}$  to apply isotropic mutations is set to 0.2 initially. This value is adapted according to the success of this operator.

In order to converge more rapidly to the final solution, we establish at each generation a quadratic approximation of the fitness in the close neighborhood of the best-so-far individual (this approximation is based on the data collected by the genetic algorithm). If the optimum of this approximation is within the specified boundaries, it replaces the last random individual scheduled for the next generation (see Appendix B of Ref. 35 for details). The data collected by the algorithm is also used to establish 2-D maps of the fitness, by using dedicated interpolation techniques. This is useful for monitoring the progress of the algorithm and for assessing the quality of the final solution.

The fitness of all individuals scheduled for the next generation is finally computed in parallel. The new population is sorted from the best individual to the worst. If the best individual of the new generation is not as good as the best individual of the previous gen-

---

<sup>1</sup>In a binary one-point crossover, the first  $n_{\text{cut}}$  bits of the DNA of the children come from one parent. The remaining  $n_{\text{bits}} - n_{\text{cut}}$  bits come from the other parent. The point  $n_{\text{cut}}$  at which the parents' DNA is exchanged is chosen randomly in the interval  $[1, n_{\text{bits}} - 1]$ .

<sup>2</sup>If  $\vec{x}_1$  and  $\vec{x}_2$  are the real variables represented by the two parents, the children obtained by a real crossover between these parents will represent a variable  $\vec{x} = \vec{x}_1 + (2 * \text{rnd} - 0.5) \times (\vec{x}_2 - \vec{x}_1)$ , where rnd is a random number uniformly distributed in  $[0,1]$ .

eration, the elite of that previous generation replaces an individual chosen at random in the new generation. We repeat these different steps from generation to generation until a termination criterion is met.

### **Quality check of the optimization results based on the plane wave number**

A final quality criterion is certainly the reliability of the presented results. In order to confirm the quality of our solutions, we increased the number of plane waves in the RCWA calculations to  $21 \times 21$  (instead of  $11 \times 11$  when running the GA). The results obtained are given in Tables 1 and 2. The comparison between  $11 \times 11$  PW and  $21 \times 21$  PW in Table 1 reveals that the solutions selected on the basis of high  $\eta$  values and high robustness are also stable with respect to this numerical test (only slight deviations between  $\eta_{11 \times 11 \text{PW}}$  and  $\eta_{21 \times 21 \text{PW}}$ ). On the contrary, the solutions in Table 2 that were discarded, essentially because of the high sensitivity of  $\eta$  with respect to the geometrical parameters, turn out to be significantly affected by this increase of the number of plane waves used in the RCWA calculations (large deviations between  $\eta_{11 \times 11 \text{PW}}$  and  $\eta_{21 \times 21 \text{PW}}$ ). It proves that the solutions given in Table 2 were rightly discarded (they fail this last reliability criterion). The fact that solutions that sit on sharp optima are also solutions that require a higher number of plane waves for an accurate calculation is actually consistent. This observation suggests a simple criterion for testing the robustness of solutions (stability with respect to deviations of their geometrical parameters): testing the stability with respect to the number of plane waves used for the calculation. This approach does not require the calculation of 2-D maps. A single calculation based on an increased number of plane waves may be sufficient to get a clue !

## **References**

- (1) Planck, M. *The theory of heat radiation*; P. Blakiston's Son & Co: Philadelphia, 1914.
- (2) Kirchhoff, G. I. On the relation between the radiating and absorbing powers of different

- bodies for light and heat. *The London, Edinburgh, and Dublin Philosophical Magazine and Journal of Science* **1860**, *20*, 1–21.
- (3) Lummer, O.; Kurlbaum, F. Der electrisch geglühte "absolut schwarze" Körper und seine Temperaturmessung. *Verhandlungen der Deutschen Physikalischen Gesellschaft* **1898**, *17*, 106–111.
- (4) Lummer, O.; Kurlbaum, F. Der elektrisch geglühte "schwarze" Körper. *Annalen der Physik* **1901**, *310*, 829–836.
- (5) Mehra, J.; Rechenberg, H. *The historical development of quantum theory*; Springer, 2000; p 39.
- (6) Barends, R. et al. Minimizing quasiparticle generation from stray infrared light in superconducting quantum circuits. *Applied Physics Letters* **2011**, *99*, 113507.
- (7) Córcoles, A.; Chow, J.; Gambetta, J.; Rigetti, C.; Rozen, J.; Keefe, G.; Rothwell, M.; Ketchen, M.; Steffen, M. Protecting superconducting qubits from radiation. **2011**, *99*, 181906.
- (8) Mizuno, K.; Ishii, J.; Kishida, H.; Hayamizu, Y.; Yasuda, S.; Futaba, D.; Yumura, M.; Hata, K. A black body absorber from vertically aligned single-walled carbon nanotubes. *Proceedings of the National Academy of Sciences* **2009**, *106*, 6044–6047.
- (9) Ishii, J.; Ono, A. A Fourier-Transform Spectrometer for Accurate Thermometric Applications at Low Temperatures. *AIP Conference Proceedings* **2003**, *684*, 705–710.
- (10) Maier, S. *Plasmonics: Fundamentals and Applications*; Springer, 2007.
- (11) Engheta, N.; Ziolkowski, R. W. *Metamaterials: physics and engineering explorations*; John Wiley & Sons, 2006.
- (12) Joannopoulos, J. D. J. D. *Photonic crystals : molding the flow of light*; Princeton University Press, 2008; p 286.

- (13) Lodahl, P.; Mahmoodian, S.; Stobbe, S. Interfacing single photons and single quantum dots with photonic nanostructures. *Reviews of Modern Physics* **2015**, *87*, 347–400.
- (14) Pendry, J. Negative refraction makes a perfect lens. *Phys. Rev. Lett.* **2000**, *85*, 3966–3969.
- (15) Pendry, J.; Smith, D. Controlling Electromagnetic Fields. *Science* **2006**, *312*, 1780–1782.
- (16) Liberal, I.; Engheta, N. Near-zero refractive index photonics. *Nature Photonics* **2017**, *11*, 149–158.
- (17) Khurgin, J. How to deal with the loss in plasmonics and metamaterials. *Nature Nanotech* **2015**, *10*, 2–6.
- (18) Landy, N.; Sajuyigbe, S.; Mock, J.; Smith, D.; Padilla, W. Perfect Metamaterial Absorber. *Phys. Rev. Lett.* **2008**, *100*, 207402.
- (19) Hedayati, M.; Javaherirahim, M.; Mozooni, B.; Abdelaziz, R.; Tavassolizadeh, A.; Chakravadhanula, V.; Zaporojtchenko, V.; Strunkus, T.; Faupel, F.; Elbahri, M. Design of a perfect black absorber at visible frequencies using plasmonic metamaterials. *Adv. Mater.* **2011**, *23*, 5410–5414.
- (20) Hedayati, M.; Faupel, F.; Elbahri, M. Tunable broadband plasmonic perfect absorber at visible frequency. *Appl. Phys. A-Mater.* **2012**, *109*, 769–773.
- (21) Cui, Y.; Fung, K.; Xu, J.; Yi, J.; He, S.; Fang, N. Exciting multiple plasmonic resonances by a double-layered metallic nanostructure. *J. Opt. Soc. Am. B* **2011**, *28*, 2827–2832.
- (22) Cui, Y.; Fung, K.; Xu, J.; He, S.; Fang, N. Multiband plasmonic absorber based on transverse phase resonances. *Opt. Express* **2012**, *20*, 17552–17559.

- (23) Zhu, P.; Guo, L. High performance broadband absorber in the visible band by engineered dispersion and geometry of a metal-dielectric-metal stack. *Appl. Phys. Lett.* **2012**, *101*, 241116.
- (24) Wang, Y.; Sun, T.; Paudel, T.; Zhang, Y.; Ren, Z.; Kempa, K. Metamaterial-plasmonic absorber structure for high efficiency amorphous silicon solar cells. *Nano Lett.* **2012**, *12*, 440–445.
- (25) Ye, Y.; Jin, Y.; He, S. Omnidirectional, polarization-insensitive and broadband thin absorber in the terahertz regime. *J. Opt. Soc. Am. B* **2010**, *27*, 498.
- (26) Cui, Y.; Fung, K.; Xu, J.; Ma, H.; Jin, Y.; He, S.; Fang, N. Ultrabroadband light absorption by a sawtooth anisotropic metamaterial slab. *Nano Lett.* **2012**, *12*, 1443–1447.
- (27) Ding, F.; Cui, Y.; Ge, X.; Jin, Y.; He, S. Ultra-broadband microwave metamaterial absorber. *Appl. Phys. Lett.* **2012**, *100*, 103506.
- (28) Argyropoulos, C.; Le, K.; Mattiucci, N.; D’Aguanno, G.; Alu, A. Broadband absorbers and selective emitters based on plasmonic Brewster metasurfaces. *Phys. Rev. B* **2013**, *87*, 205112.
- (29) Qiuqun, L.; Weixing, Y.; Wencai, Z.; Taisheng, W.; Jingli, Z.; Hongsheng, Z.; Shaohua, T. Numerical study of the meta-nanopyramid array as efficient solar energy absorber. *Opt. Mater. Express* **2013**, *3*, 1187–1196.
- (30) Zhou, Y.; Qin, Z.; Liang, Z.; Meng, D.; Xu, H.; Smith, D. R.; Liu, Y. Ultra-broadband metamaterial absorbers from long to very long infrared regime. *Light: Science & Applications* **2021**, *10*, 138.
- (31) Dixon, K.; Montazeri, A. O.; Shayegannia, M.; Barnard, E. S.; Cabrini, S.; Mat-

- suura, N.; Holman, H.-Y.; Kherani, N. P. Tunable rainbow light trapping in ultrathin resonator arrays. *Light: Science & Applications* **2020**, *9*, 138.
- (32) Hajian, H.; Ghobadi, A.; Butun, B.; Ozbay, E. Active metamaterial nearly perfect light absorbers: a review. *J. Opt. Soc. Am. B* **2019**, *36*, F131–F143.
- (33) Huang, J.; Liu, C.; Zhu, Y.; Masala, S.; Alarousu, E.; Han, Y.; Fratilocchi, A. Harnessing structural darkness in the visible and infrared wavelengths for a new source of light. *Nature Nanotechnology* **2016**, *11*, 60–66.
- (34) Ziegler, M.; Dathe, A.; Pollok, K.; Langenhorst, F.; Hübner, U.; Wang, D.; Schaaf, P. Metastable Atomic Layer Deposition: 3D Self-Assembly toward Ultradark Materials. *ACS Nano* **2020**, *14*, 15023–15031.
- (35) Mayer, A.; Lobet, M. UV to near-infrared broadband pyramidal absorbers via a genetic algorithm optimization approach. *Proc. SPIE* **2018**, *10671*, 1067127–1–11.
- (36) Mayer, A.; Griesse-Nascimento, S.; Bi, H.; Mazur, E.; Lobet, M. Optimization by a genetic algorithm of pyramidal structures made of one, two or three stacks of metal/dielectric layers for a quasi-perfect broadband absorption of UV to near-infrared radiations. *Proc. SPIE* **2020**, *11344*, 113441L–1–13.
- (37) Liu, C.; Maier, S.; Li, G. Genetic-Algorithm-Aided Meta-Atom Multiplication for Improved Absorption and Coloration in Nanophotonics. *ACS Photonics* **2020**, *7*, 1716–1722.
- (38) Gong, M.; Kim, H.; Larsson, J.; Methling, T.; Alden, M.; Kristensson, E.; Brackmann, C.; Eschrich, T.; Jager, M.; Kiefer, W.; Ehn, A. Fiber-based stray light suppression in spectroscopy using periodic shadowing. *Opt. Express* **2021**, *29*, 7232–7246.
- (39) Fest, E. *Stray Light Analysis and Control*; SPIE, 2013.

- (40) Clapham, P.; Hutley, M. Reduction of lens reflexion by the moth eye principle. *Nature* **1973**, *244*, 281–282.
- (41) Deparis, O.; Vigneron, J.-P.; Agustsson, O.; Decroupet, D. Optimization of photonics for corrugated thin-films solar cells. *J. Appl. Phys.* **2009**, *106*, 094505.
- (42) Prodan, E.; Radloff, C.; Halas, N.; Nordlander, P. A hybridization model for the plasmon response of complex nanostructures. *Science* **2003**, *302*, 419–422.
- (43) Christ, A.; Zentgraf, T.; Tikhodeev, S.; Gippius, N.; Kuhl, J.; Giessen, H. Controlling the interaction between localized and delocalized surface plasmon modes: experiment and numerical calculations. *Phys. Rev. B* **2006**, *74*, 155435.
- (44) Liu, N.; Guo, H.; Fu, L.; Kaiser, S.; Schweizer, H.; Giessen, H. Plasmon hybridization in stacked cut-wire metamaterials. *Adv. Mater.* **2007**, *19*, 3628–3632.
- (45) Pu, M.; Feng, Q.; Hu, C.; Luo, X. Perfect absorption of light by coherently induced plasmon hybridization in ultrathin metamaterial film. *Plasmonics* **2012**, *7*, 733–738.
- (46) Lobet, M.; Lard, M.; Sarrazin, M.; Deparis, O.; Henrard, L. Plasmon hybridization in pyramidal metamaterials: a route towards ultra-broadband absorption. *Opt. Express* **2014**, *22*, 12678–12690.
- (47) Lobet, M.; Henrard, L. Metamaterials for ultra-broadband super absorbers based on plasmon hybridization. 8th International Congress on Advanced Electromagnetic Materials in Microwaves and Optics. 2014; pp 190–192.
- (48) Beadie, G.; Brindza, M.; Flynn, R.; Rosenberg, A.; Shirk, J. Refractive index measurements of poly(methyl methacrylate) (PMMA) from 0.4-1.6  $\mu\text{m}$ . *Appl. Optics* **2015**, *54*, 139.
- (49) Johnson, P.; Christy, R. Optical constants of noble metals. *Phys. Rev. B* **1972**, *6*, 4370–4379.

- (50) Johnson, P.; Christy, R. Optical constants of transition metals: Ti, V, Cr, Mn, Fe, Co, Ni, and Pd. *Phys. Rev. B* **1974**, *9*, 5056–5070.
- (51) Rakic, A. Algorithm for the determination of intrinsic optical constants of metal films: application to aluminum. *Appl. Optics* **1995**, *34*, 4755.
- (52) Rakic, A.; Djuricic, A.; Elazar, J.; Majewski, M. Optical properties of metallic films for vertical-cavity optoelectronic devices. *Appl. Optics* **1998**, *37*, 5271–5283.
- (53) Dennis Jr., J.; Schnabel, R. B. *Numerical Methods for Unconstrained Optimization and Nonlinear Equations*; SIAM: Philadelphia, 1996.
- (54) Goldberg, D. *Genetic Algorithms in Search, Optimization and Machine Learning*; Addison-Wesley: Reading, Mass., 1989.
- (55) Haupt, R.; Werner, D. *Genetic Algorithms in Electromagnetics*; J. Wiley & Sons: Hoboken, NJ, 2007.
- (56) Eiben, A.; Smith, J. *Introduction to Evolutionary Computing*, 2nd ed.; Springer-Verlag: Berlin, 2007.
- (57) Kennedy, J.; Eberhart, R. Particle Swarm Optimization. *Proceedings of ICNN'95 - International Conference on Neural Networks* **1995**, *4*, 1942–1948.
- (58) Shi, Y.; Eberhart, R. A Modified Particle Swarm Optimizer. *Proceedings of IEEE International Conference on Evolutionary Computation* **1998**, 69–73.
- (59) Bonyadi, M.; Michalewicz, Z. Particle swarm optimization for single objective continuous space problems: a review. *Evolutionary Computation* **2017**, *25*, 1–54.
- (60) Dorigo, M.; Stützle, T. *Ant Colony Optimization*; MIT Press: Cambridge, MI, 2004.



- (61) Gaier, A.; Asteroth, A.; Mouret, J.-B. Discovering Representations for Black-box Optimization. *Proceedings of the Genetic and Evolutionary Computation Conference (GECCO '20)* **2020**, 103–111.
- (62) Moharam, M.; Gaylord, T. Rigorous coupled-wave analysis of planar-grating diffraction. *J. Opt. Soc. Am. A* **1981**, *71*, 811–818.
- (63) Khurgin, J. Replacing noble metals with alternative materials in plasmonics and metamaterials: how good an idea? *Phil. Trans. R. Soc. A* **2017**, *375*, 20160068.
- (64) Brenner, K.-H. Aspects for calculating local absorption with the rigorous coupled-wave method. *Opt. Express* **2010**, *18*, 10369–10376.

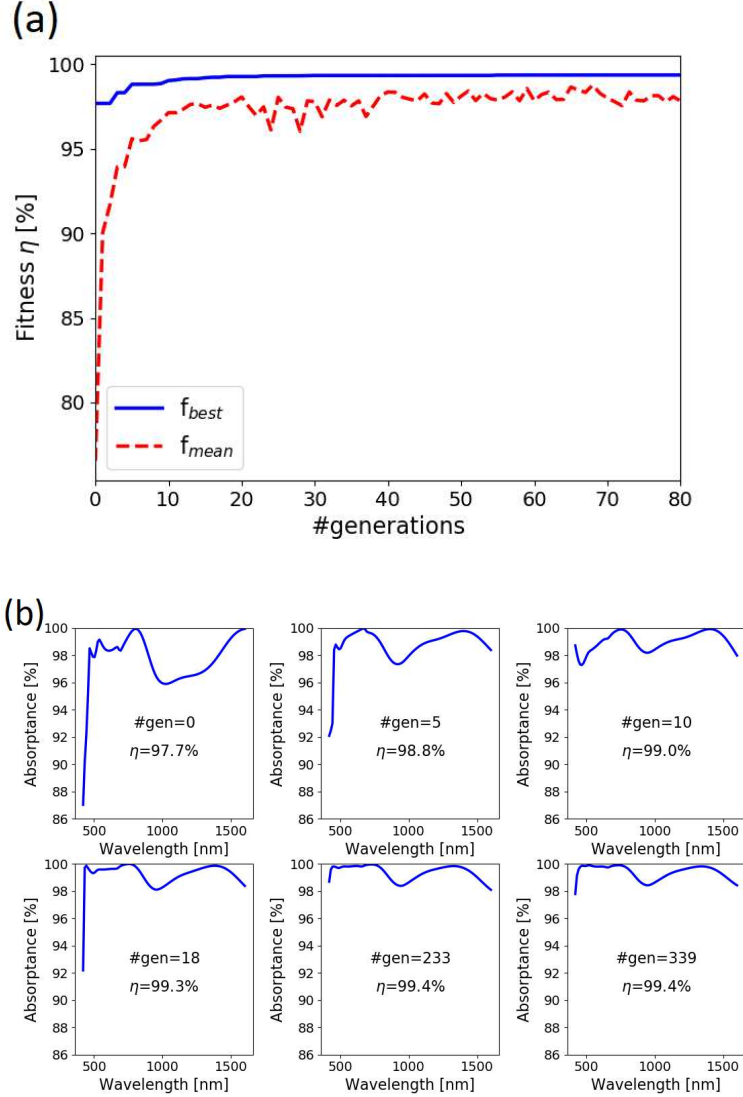


Figure 3: (a) best fitness (solid) and mean fitness (dashed) in the first 80 generations when optimizing  $N = 3$  stacks of W/PMMA. (b) Absorbance spectrum for the best solution obtained after 0, 5, 10, 18, 233 and 339 generations. The genetic algorithm was run with a population  $n_{pop}$  of 50 individuals. The final solution has a fitness  $\eta$  of 99.4% when using  $11 \times 11$  PW in the RCWA calculations.

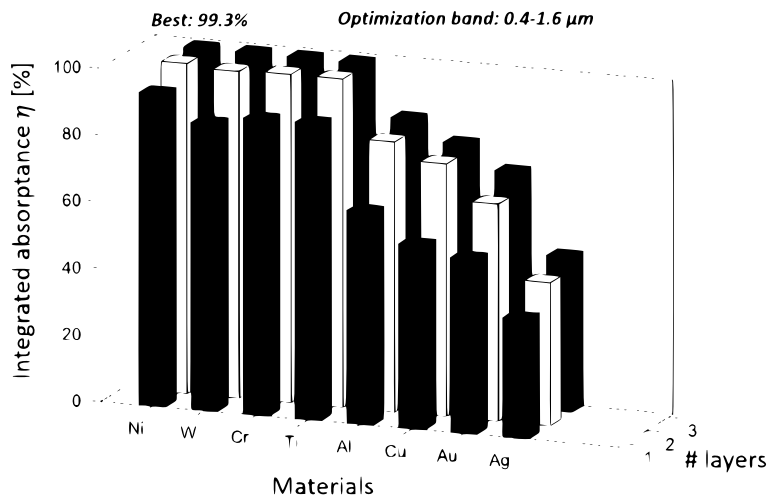


Figure 4: Figure of merit (integrated absorbance)  $\eta$  achieved for each structure considered. These results correspond to RCWA calculations with  $21 \times 21$  plane waves.

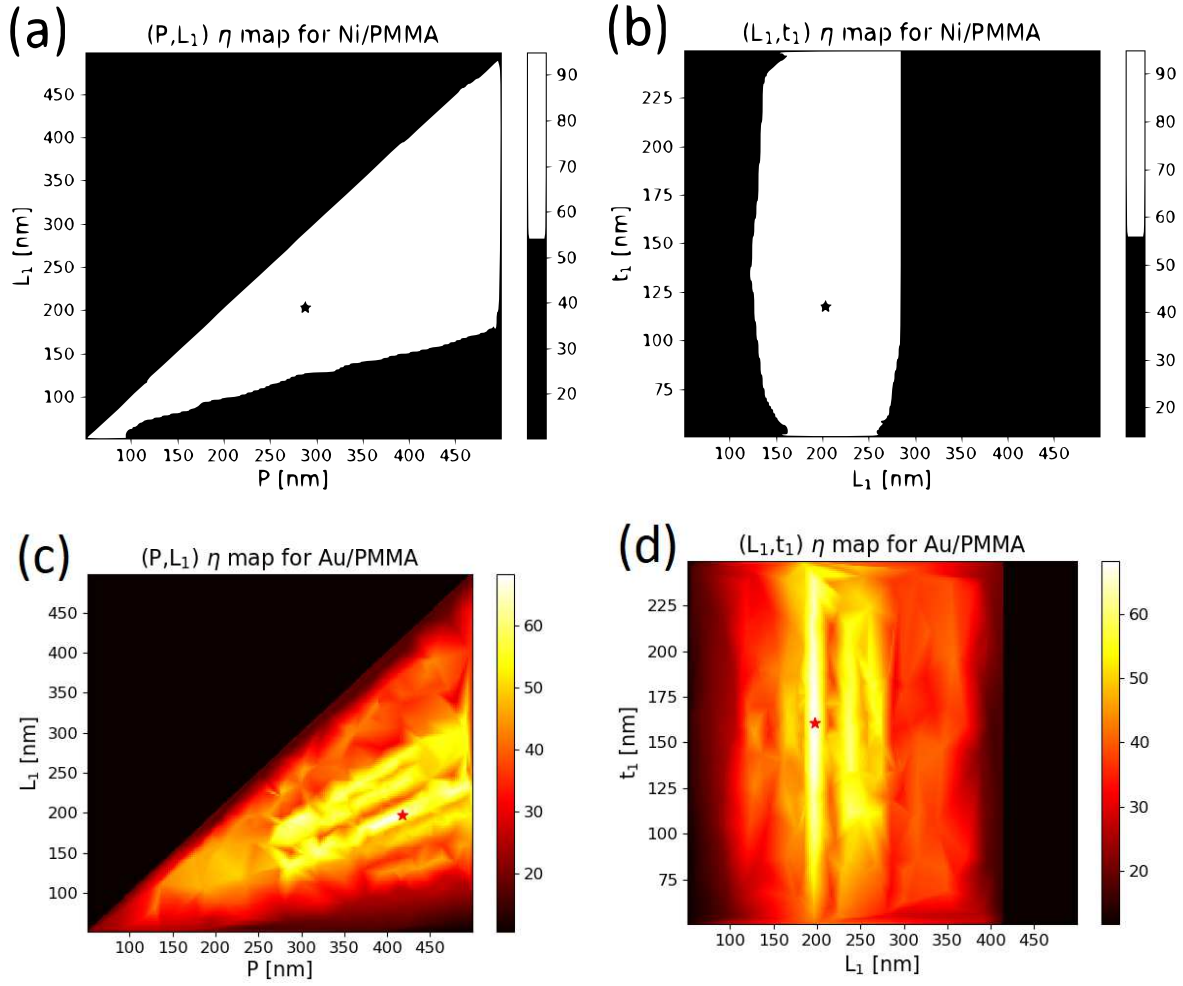


Figure 5: Maps obtained by a linear interpolation of the data collected by the genetic algorithm in the  $(P, L_1)$  and  $(L_1, t_1)$  planes that include the final solution established by the algorithm (indicated by a star). (a)-(b) optimization of 1 stack of Ni/PMMA (global optimum at  $P=286$  nm,  $L_1=201$  nm and  $t_1=117$  nm). (c)-(d) optimization of 1 stack of Au/PMMA (global optimum at  $P=416$  nm,  $L_1=196$  nm and  $t_1=160$  nm).

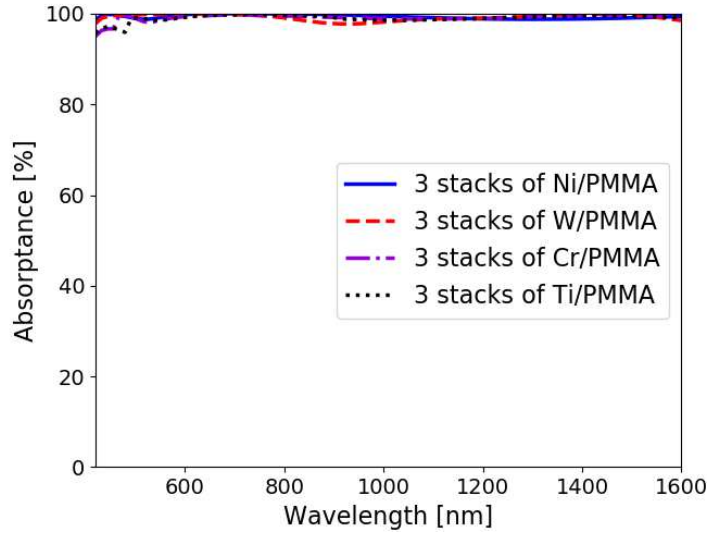


Figure 6: Absorptance spectrum for optimized structures made of  $N = 3$  stacks of Ni/PMMA (solid), W/PMMA (dashed), Cr/PMMA (dot-dashed) and Ti/PMMA (dotted). These results correspond to a normally incident radiation and RCWA calculations using  $21 \times 21$  plane waves.

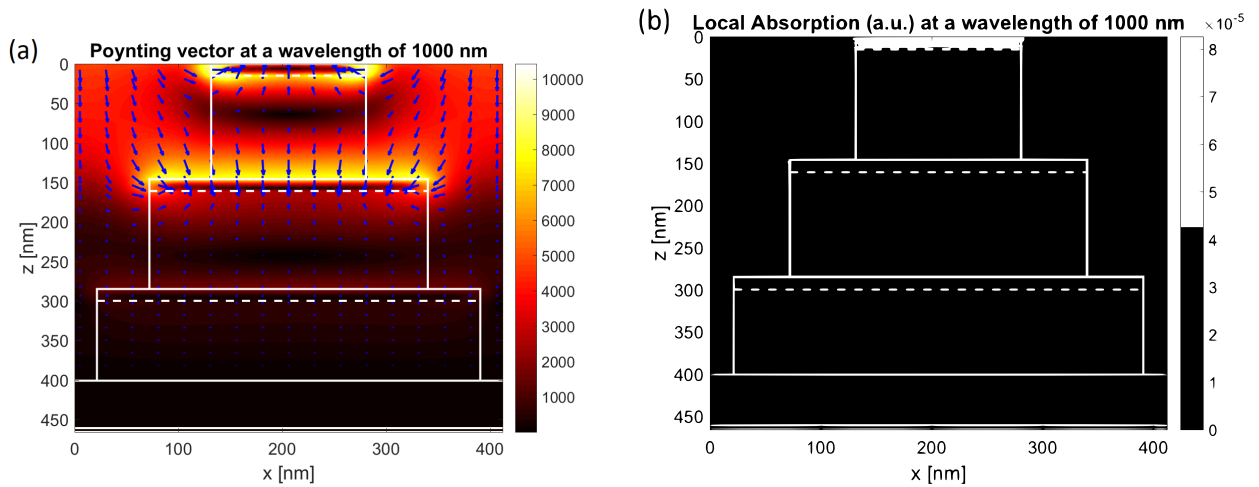


Figure 7: (a) Time-averaged Poynting vector and (b) time-averaged local absorption in the central  $(x, z)$  plane of a structure made of  $N = 3$  stacks of Ni/PMMA for a normally incident radiation at a wavelength of 1000 nm.

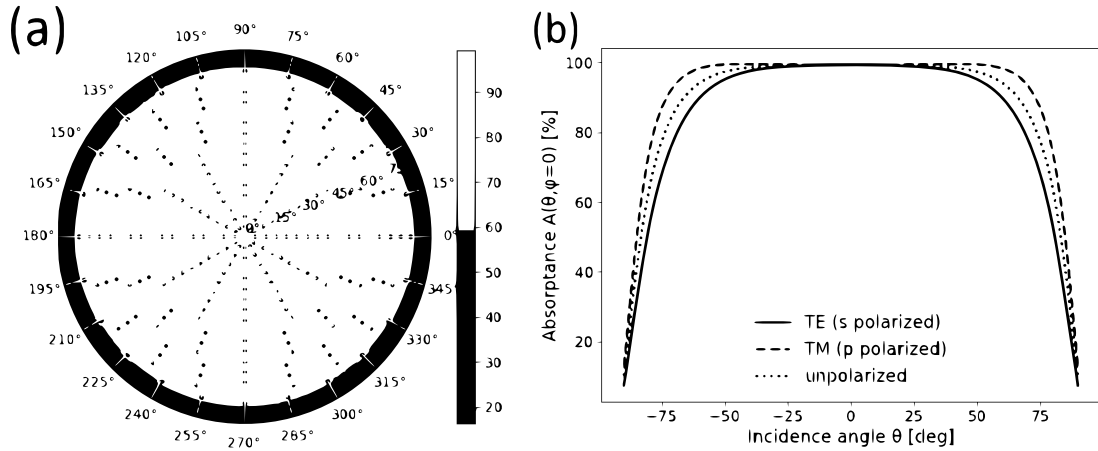


Figure 8: Integrated absorptance for  $N=3$  stacks of Ni/PMMA (results obtained with  $21 \times 21$  plane waves). Left: integrated absorptance for an unpolarized incident radiation, as a function of the polar and azimuthal angles  $\theta$  and  $\phi$ . The blue points show the  $(\theta, \phi)$  values for which an explicit RCWA calculation was performed; these points are used in a cubic interpolation to generate a 2-D map. Right: integrated absorptance for a TE (s polarized), a TM (p polarized) and an unpolarized incident radiation, as a function of  $\theta$  with  $\phi = 0$  (horizontal profile).

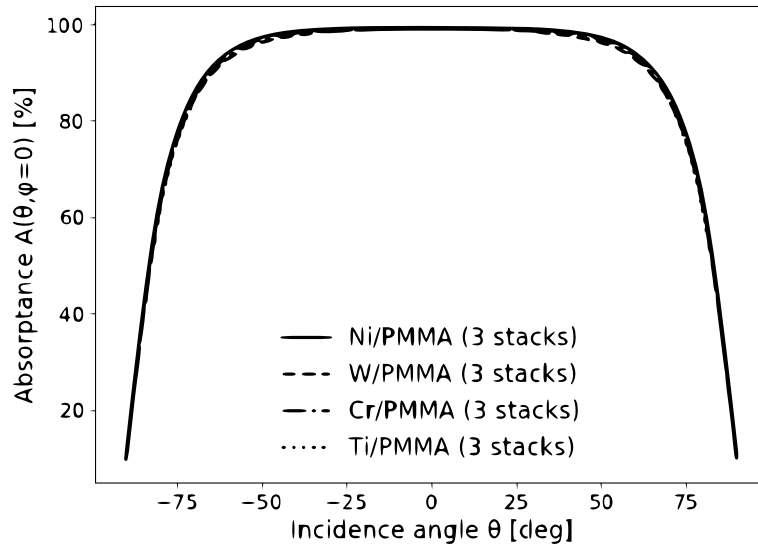


Figure 9: Integrated absorptance for an unpolarized incident radiation with polar angle  $\theta \in [-90^\circ, 90^\circ]$  and azimuthal angle  $\phi = 0^\circ$  (horizontal profile). The results correspond to  $N=3$  stacks of Ni/PMMA (solid), W/PMMA (dashed), Cr/PMMA (dot-dashed) and Ti/PMMA (dotted). These results are obtained with  $21 \times 21$  plane waves.